DOI: 10.1002/((please add manuscript number))

Article type: Research Article

Dual-functional Perovskite-based Photodetector and Memristor for Visual Memory

Fa Cao, Zijun Hu, Tingting Yan, Enliu Hong, Xiaolei Deng, Limin Wu* and Xiaosheng Fang*

Dr. F. Cao, Z.J. Hu, T.T. Yan, E. L. Hong, Dr. X. L. Deng, Prof. L. M. Wu and Prof. X. S. Fang

Department of Materials Science, State Key Laboratory of Molecular Engineering of Polymers

Fudan University

Shanghai 200433, P. R. China

E-mail: xshfang@fudan.edu.cn (X. S. Fang)

Prof. L. M. Wu

College of Chemistry and Chemical Engineering Inner Mongolia University Hohhot 010021, P. R. China

E-mail: lmw@fudan.edu.cn (L. M. Wu)

Abstract

The imitation of human visual memory, which demands the multifunctional integration of light sensors similar to the eyes, and image memory, similar to the brain. Although humans have already implemented electronic devices with visual memory functions, these devices require a combination of various components and logical circuits. With the advancement of integrated circuits, the miniaturization and high integration of devices are an inevitable trend. Therefore, the combining of visual perception and high-performance information storage capabilities into a single device to achieve visual memory remains a challenging. In this study, inspired by the function of human visual memory, we designed a dual-functional perovskite-based photodetector (PD) and memristor to realize visual perception and memory capacities. As a PD, it realized an ultra-high self-powered responsivity of 276 mAW^{-1}, a high detectivity of 4.7×10^{11} Jones (530 nm; light intensities, 2.34 $mWcm^{-2}$), and a high rectification ratio of ~100 (± 2V). As a memristor, an ultra-high on/off ratio (~10^5), an ultra-low power consumption of 3×10^{-11} W, a low setting voltage (0.15 V), and a long retention time (>7000 s) were realized. Moreover, the dual-functional device has the capacity to perceive and remember light paths and store data with good cyclic stability. Our device exhibits perceptual and cyclic erasable memory functions, which provide new opportunities for mimicking human visual memory in future multifunctional applications.

Keywords: Dual-functional; perovskite; photodetector; memristor; visual memory

1. Introduction

Human visual memory is achieved through the perception of surrounding objects by the eyes and is transmitted through nerve fibers to the memory center of the brain.[1–3] The visual systems can perceive and respond to the complex external environments, and more than 80% of the information from our surroundings is processed and transmitted to the brain via a visual perception system. The new era of artificial intelligence (AI) and Internet of Things (IoT) call for an intelligent system comprising the central nervous system for computing and memory, and visual system for the information detection of stimuli from the external environment. Such systems should exhibit low energy consumption and high parallel–processing power, similar to the human visual memory system.[4–7]

Recent research has realized a recognition function for perceiving images by utilizing image–sensor arrays. However, few studies have focused on the capacity to memorize image information after removing the external image stimulation.[2, 8–10] Recently, emerging optoelectronic artificial synapses have realized the capacity of light sensing and memory; however, such devices typically have shorter memory times. For example, various two-terminal and self-powered optoelectronic synaptic devices based on lead-free perovskite have been successfully fabricated, including $Cs_3Bi_2Br_9$ and $Cs_2AgBiBr_6$, which exhibit a memory time of less than 70 s.[11] To solve the problem of short memory time, researchers have integrated photosensitive devices and the nonvolatile resistive random-access memory (RRAM, a newly emerging memristor with low energy consumption and high computing speed constructed using simple metal/insulator/metal thin-film stacks) devices into a single system. For instance, Shen et al. designed a facile architecture of visual memory arrays to mimic the human visual memory by integrating ultraviolet (UV) image sensor arrays and resistance switching memristors in a series.[1] However, the integration of different devices increases the preparation difficulty and reduces the degree of integration of the visual memory system. Even an Ag/PMMA/$Cs_2AgBiBr_6$/ITO memristor, which can be reset by UV light, realizing the function of human visual memory.[12] Nevertheless, it can not be separately used as an photodetector (PD). Therefore, a highly integrated device that is

similar to the human visual memory system is urgently needed for application in AI, IoT and other application scenarios

Perovskites, a newly emerging materials, has exhibited great application prospects in solar cells, light-emitting diodes, PDs and memristors.[12–16] For example, a filter-less color/spectrum-sensitive $MAPbX_3$ perovskite PD with ultrahigh-speed response and high spectral resolution has been reported.[17] A fast and reliable RRAM that based on $CsPbBr_3$ perovskite quantum dots (QDs) was constructed, which lead to more powerful perovskite-based memristor devices.[18] Early developments mostly focused on Pb-based perovskite materials. However, to our knowledge, dual-functional Pb-based perovskite is rarely reported, and the toxicity of Pb limits their further utilization. Recently, a stable and environmentally friendly $A_3M_2X_9$ (M= Bi^{3+}, Sb^{3+} and X= I, Br etc.) perovskite-like structure was proposed. For example, $Cs_3Bi_2I_9$, $Cs_3Bi_2Br_9$, $Cs_3Sb_2I_9$, and $Cs_3Sb_2Br_9$ have shown good performance either in PD or memristors.[19–22] However, there have been no report on dual-functional devices based on the lead-free perovskites. Inspired by the multifunctional characteristics of perovskite materials, designing a dual-functional device with the ability of photoelectric detection and memristor functions will realize the target of human visual memory function. Furthermore, dual-functional devices can satisfy the requirements of increasingly highly integrated circuits.

In this study, a dual-functional $Cs_3Sb_2I_9$ perovskite-based PD and memristor, realizing visual perception and memory capacities, was demonstrated. An ultra-high self-powered responsivity of 276 mAW^{-1} and a high detectivity of 4.7×10^{11} Jones as a PD and an ultra-high on/off ratio (~10^5), an ultra-low power consumption of 3×10^{-11} W, a low setting voltage (0.15 V), and a long retention time (>7000 s) as a memristor were realized by the dual-functional device. Such devices provide new opportunities for mimicking the human visual memory in future multifunctional applications.

2. Results and Discussion

Figure 1 shows a human visual memory system and our dual-functional perovskite-based PD and memristor with the capacities of visual perception and memory capacities. Human visual memory is formed by the eyes (receiving image information), the optic nerves (signal transmission), and the

brain (processing the neural signals), enabling high-speed visual processing and recognition[23](Figure 1a). To achieve visual memory, a light sensor, an image memory device, and a logical circuit must be integrated into one system, which complicates the fabrication process. In this study, we designed a dual-functional device with visual sensing and memory abilities to provide new opportunities for mimicking the human visual memory. To demonstrate the capabilities of the dual-functional self-powered PD and memristor for imaging and memorization, a 4 × 4 arrays was fabricated to record the information. A moving light source followed the direction indicated by the arrow in Figure 1b. When the light source passed through, the corresponding pixel generated an enhanced photocurrent. Then, the pixels that generated the photocurrent in sequence were recorded and set in a low resistance state (recorded as "1"), to enable recording the path of the light. Moreover, a series of modulated light sources irradiated different pixels (red circles in Figure 1c), setting the pixel that generated the photocurrent to a low-resistance state. By defining the pixels in the low impedance state (~ 10^{-6} A) as "1" and those in the high impedance state (~ 10^{-11} A) as "0," data storage was achieved. To further imitate the human visual memory, a beam of Z-shaped

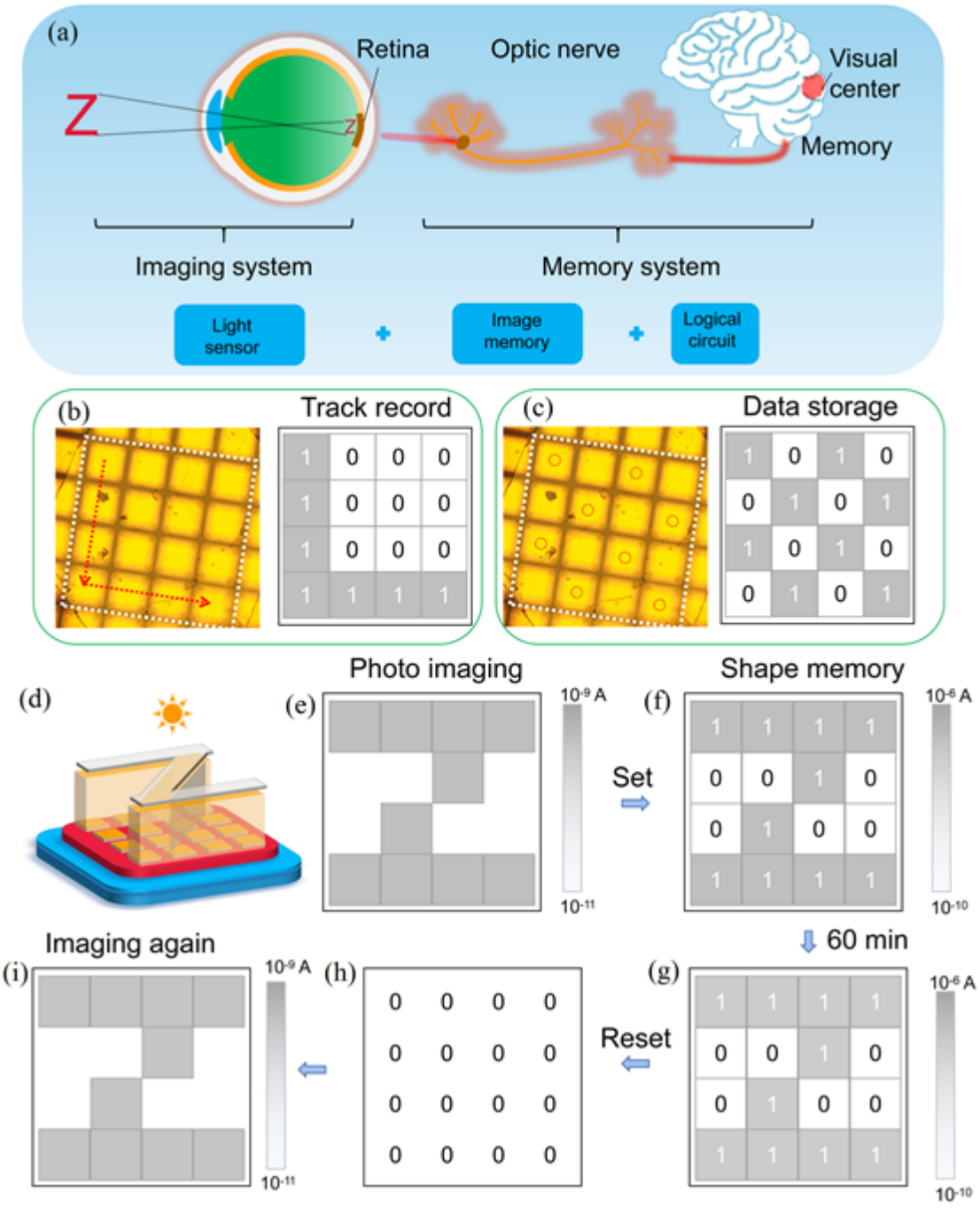

Figure 1 **a)** Schematic of the human visual system when the Z shape was observed by the eyes. **b)** Schematic of the route of light and the corresponding track recording results (50 × 50 μm for each single pixel). **c)** Schematic of the photoelectric writing and the corresponding data storage results. **d)** Schematic of 4 × 4 arrays Au/Ag-$Cs_3Sb_2I_9$-ITO (indium tin oxide films) dual-functional devices. **e)**

The photo imaging result of the device (light intensity: 2.34 $mWcm^{-2}$). **f, g)** The data storage and shape memory of the image before and after 60 min. **h)** The result of the array after reset. **i)** The photo imaging result of the device after resetting.

light (530 nm; 2.34 $mWcm^{-2}$) was illuminated on the 4 × 4 arrays, as shown in Figure 1d. Current-time (I-T) tests revealed that all device units had a dark current with an average value of ~ 10^{-11} A, and an average photocurrent value of ~ 4 ×10^{-9} A (530 nm; 0 V). After measurement of all pixels, the results were described by a 2D current contrast map, as observed in Figure 1e. The "Z" shape could be clearly identified when the device was illuminated by 530 nm light, realizing the photoimaging ability similar to the eyes. To remember the Z-shape, we set all the pixels in the Z-shaped zone to the low-impedance state, while the other pixels were maintained in the high-impedance state (Figure 1f). After 60 minutes, all the pixels were read under 0.01 V bias, and it is clearly that the pixels in the Z-shaped zone were still in the low-impedance state. Thus, we realized the image memory capacity of the device which is similar to the brain (Figure 1g). After applying a reverse scan voltage from -0.5 to 0 V to reset all pixels (Figure 1h), the device still exhibited an excellent optical imaging ability (Figure 1i). These results provide a novel concept for inmitating the human visual memory that has tremendous commercial value.

A schematic of the fabrication of $Cs_3Sb_2I_9$ micro-plates under different confining pressures is shown in Figure 2a, and the corresponding optical images are shown in Supporting Information Figure S1. The average thickness and size of the $Cs_3Sb_2I_9$ micro-plates under different confining pressures are shown in Figure 2b and c, and the corresponding optical images are shown in Figures S2 and Figure S3. By increasing the confining pressure from 0 to 120 N (0 to 2F), the thickness of the micro-plates decreased from 6.1 to 0.8 μm, while the average size increased from 180 to 600 μm; the highest size the micro-plates could reach was ~1 mm, as shown in the optical image in Figure S3-2F. Increasing the confining pressure decreased the distance between the substrate and hydrophobic glass, which limited the longitudinal growth of the micro-plates and promoted their transverse growth, as shown in the schematic diagram of growth in different confined spaces in Figure S4. Thus, the size of the micro-plates could be controlled by adjusting the confining pressure.

The X-ray diffraction (XRD) patterns of the as-fabricated $Cs_3Sb_2I_9$ micro-plates are shown in Figure 2d. The diffraction peaks with 2θ of 16.98, 25.69, 30.22, 43.44, and 52.66°

were indexed to the (002), (003), (022), (005), and (006) crystal facets of the hexagonal phase $Cs_3Sb_2I_9$ (JCPDF 88-0690). The XRD pattern showed dominant diffraction peaks corresponding to the (003) and (006) planes of $Cs_3Sb_2I_9$, indicating that the crystal was in the pure phase and (00l)-oriented. Figures 2e–h show the scanning electron microscopy (SEM) images of the $Cs_3Sb_2I_9$ micro-plates and energy dispersive spectroscopy mappings of Cs, Sb, and I elements with a confining pressure of 60 N. The $Cs_3Sb_2I_9$ micro-plates exhibited a lateral length of ~450 µm, and the Cs, Sb, and I elements (with atomic ratio of 21.3, 14.2 and 64.5 %; Cs : Sb : I = 21.3 :14.2 :64.5 ≈ 3 :2 :9) were distributed uniformly in the $Cs_3Sb_2I_9$ micro-plates, which indicates that no observable impurity was present. The surface roughness of a $Cs_3Sb_2I_9$ micro-plate is shown in Figure 2i. The average roughness of the $Cs_3Sb_2I_9$ micro-plate was 2.3 nm, demonstrating its high smoothness. Focused ion beam prepared ITO-$Cs_3Sb_2I_9$-Ag/Au samples were used to show the original crystal structure of $Cs_3Sb_2I_9$ and the contacting interface. As shown in Figure 2j, the ITO and $Cs_3Sb_2I_9$ micro-plates showed a high-quality contacting interface, and there were no defects such as voids present. Figure 2k shows a high-resolution transmission electron microscopy (TEM) image of the $Cs_3Sb_2I_9$ micro-plate. The lattice spacings of 0.237 nm and 0.236 nm are assigned to the (220) and (204) inter-planar spacings of the $Cs_3Sb_2I_9$ micro-plate, respectively. The corresponding fast Fourier transform analysis (Figure 2l) of the TEM images was performed. The periodic diffraction spots indicate the high single crystallinity of the $Cs_3Sb_2I_9$ micro-plates.

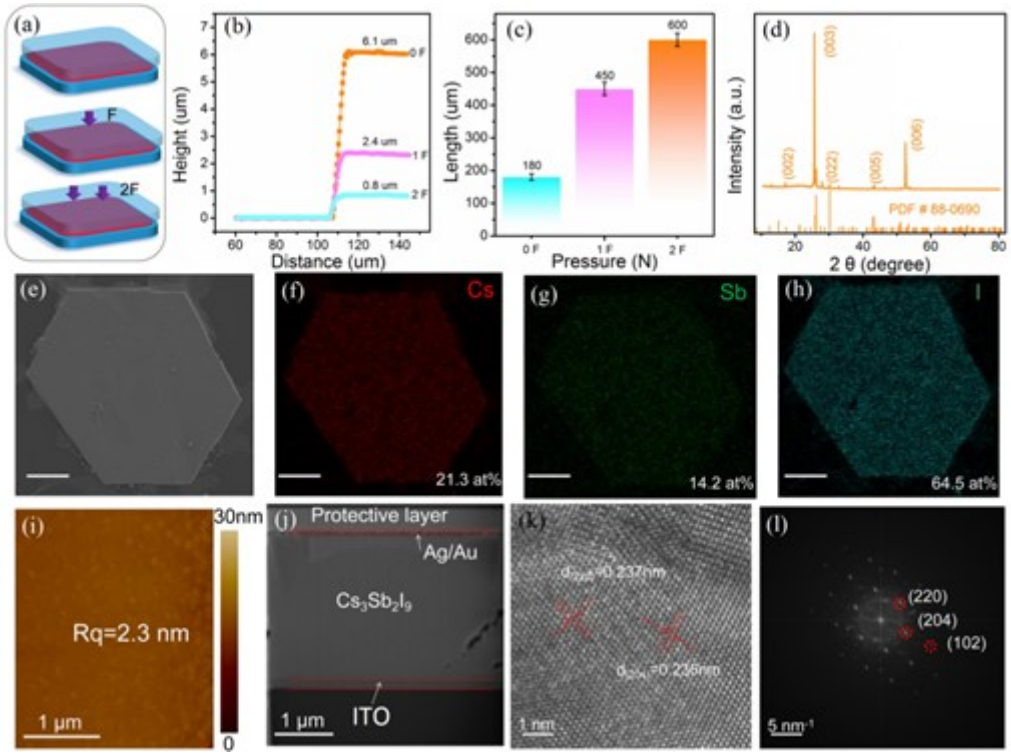

Figure 2 **a)** Schematic of the growth condition under different pressures (F = 60 N) and **b, c)** are the average thickness and size of the micro-plates under different confining pressures (0, 60, and 120 N). **d)** X-ray diffraction pattern of $Cs_3Sb_2I_9$ micro-plates. **e**–**h)** Scanning electron microscopy image of $Cs_3Sb_2I_9$ micro-plates (scale bar 100 μm) and the corresponding energy dispersive spectroscopy mappings of Cs, Sb and I **i)** Atomic force microscopy image corresponding to **e)**. **j)** Cross sectional transmission electron microscopy (TEM) image of ITO-$Cs_3Sb_2I_9$-Ag/Au. **k, l)** High-resolution TEM image and the corresponding fast Fourier transform patterns of $Cs_3Sb_2I_9$.

First-principle calculations using the density functional theory toward the band structures were performed to gain insights into the electronic and optical properties of the $Cs_3Sb_2I_9$ micro-plate.[24, 25] Figure 3a shows a schematic diagram of the crystal structure of the $Cs_3Sb_2I_9$ perovskite, in which the unit cell consists of bi-octahedral $(Sb_2I_9)^{3-}$ clusters that are surrounded by Cs cations to achieve the charge balance. The unit cell has a trigonal phase with lattice parameters of a = b = 8.42 Å and c = 10.386 Å, and angles of α = β = 90° and γ = 120°. The calculated band structures of the $Cs_3Sb_2I_9$ micro-plate are shown in Figure 3b and indicate a nearly direct band gap of 2.05 eV. There was little difference between the direct

and indirect band gaps of this material, which is consistent with the previous reports.[24, 25] The total and partial density of states plots show that the valence band maximum (VBM) of the $Cs_3Sb_2I_9$ micro-plate mainly contributed by the interactions of I 5p and Sb 5s, whereas the conduction band minimum (CBM) was dominated by the I 5p and Sb 6p interactions, as illustrated in Figure 3c. Figure 3d shows the UV-vis absorption and photoluminescence (PL) spectra of the $Cs_3Sb_2I_9$ micro-plate. Based on the absorption spectrum, the $Cs_3Sb_2I_9$ micro-plate exhibited a stepwise absorption feature with an absorption edge located at ~530 nm, which can be considered as the 1st exciton absorption peak. No absorption tails or exciton features were observed, demonstrating the high crystalline quality of the $Cs_3Sb_2I_9$ micro-plate. The PL peak of the micro-plate is located at 646 nm. In this case, there was a strong Stokes shift of approximately 0.42 eV between the absorption edge and the PL emission. The band gap of the $Cs_3Sb_2I_9$ micro-plate afforded a value of ~2.04 eV, estimated according to the Tauc equation[26], as illustrated in Figure 3e. Figure 3f displays the high-resolution X-ray photoelectric spectroscopy (XPS) valance band (defined as the energy bandgap from the Fermi level to the VBM) spectrum of the $Cs_3Sb_2I_9$ micro-plate. The valence band of the $Cs_3Sb_2I_9$ micro-plate is 0.70 eV. This result shows that the Fermi level was close to the VBM, demonstrating the p-type conductivity of the $Cs_3Sb_2I_9$ micro-plate. Furthermore, Kelvin probe force microscope tests were performed to confirm the Fermi level of the micro-plate. Before the test, the micro-plate was evaporated with a 50 nm Au film for work function calibration. Figures 3g and h show a clear step between Au (the left part of the micro-plate) and $Cs_3Sb_2I_9$. With Au calibration (work function ~ 5.1 eV), it has been validated that the work function of $Cs_3Sb_2I_9$ is 5.05 eV, since its surface potential increases by approximately 0.05 V compared with Au. Based on the above energy level analysis, the position of the VBM is calculated to be 5.75 eV (5.05 + 0.7 eV), and the position of the CBM is 3.71 eV (5.75 - 2.04 eV). A schematic of the energy is shown in Figure 3i.

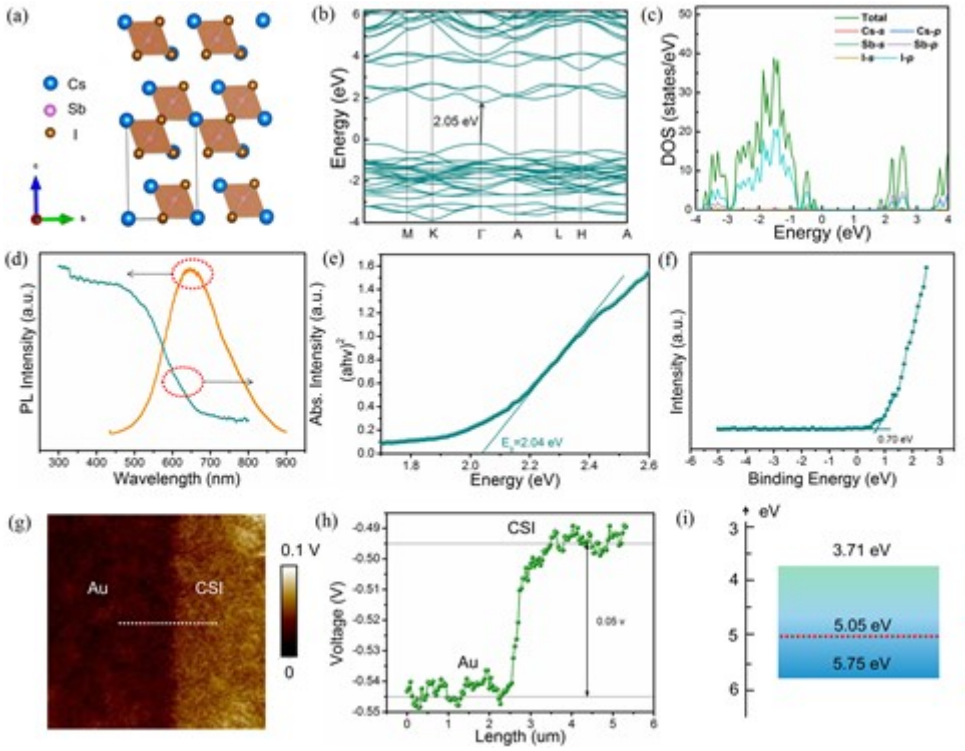

Figure 3 **a)** The crystal unite cell structure. **b)** Heyd–Scuseria–Ernzerhof calculated band structures of $Cs_3Sb_2I_9$ and **c)** the corresponding density of states. **d)** Absorption spectrum (right axis) and photoluminescence spectrum (left axis) for $Cs_3Sb_2I_9$ microplates. **e)** the band gap of $Cs_3Sb_2I_9$ obtained from the absorption spectrum. **f)** Valence band spectrum of $Cs_3Sb_2I_9$ micro-plates. **g,h)** Kelvin probe force microscope results of $Cs_3Sb_2I_9$ microplates. **i)** Energy band alignment of $Cs_3Sb_2I_9$ micro-plates.

Figure 4a schematically shows the device structure of the $Cs_3Sb_2I_9$-based PD, and the corresponding vertical structure is shown in Figure S5. The PD1 with channel materials of $Cs_3Sb_2I_9$ ($Cs_3Sb_2I_9$ micro-plate thickness of ~2.4 μm) were fabricated, where Au/Ag was deposited as top electrode and ITO acts as the bottom electrode. The corresponding current-voltage (I-V) curves of the ITO-$Cs_3Sb_2I_9$-Ag/Au PD under dark conditions and under 530 nm light illumination are shown in Figure 4b. The rectification behavior of the I-V curves under dark condition was caused by the asymmetric electrodes, and a high rectification ratio of ~100 (± 2V) was achieved. The enhanced photocurrent of the I-V curves under 530 nm light at a 0 V bias demonstrates its high self-powered photodetection abilities. During the second I-V test under light conditions, the significantly enhanced current (from 10^{-8} to 10^{-5} A) at a 2 V bias was attributed to the electroforming of the conductive

filament, which will be discussed in the memristor section. The PD1 showed lower dark current than PD2 ($Cs_3Sb_2I_9$ micro-plate thickness of ~0.8 μm) when its I-V curves (Figure 4b) was compared with the I-V curves of PD2 (Figure S6), which was caused by the large resistance of PD1, leading to the better performance of PD1. Figure 4c shows the time-dependent (I-T) photoresponse of the PD1 under various incident light intensities at a 0 V bias. A prompt and regular rectangular photoresponse curve with good cycling stability was distinctly observed, and the photo current increased with increasing light intensities from 0.49 to 2.34 mW cm^{-2}. This was due to an increase of photogenerated carriers, which correlated with the absorbed photon flux. In Figure 4d, the curve of the photocurrents varying with the incident light power densities is fitted with the power-law:[27] $I \sim P^{\theta}$. The exponent θ ($0.5 < \theta < 1$) determines the response of the photocurrent to light intensity, depending on the processes of electron-hole generation, trapping, and recombination. A good linear relationship with the best-fit curve yielded a nearly linear behavior of $\theta = 0.82$. This nearly linear behavior indicates that the PD1 is capable of detecting light intensities within a wide range. The responsivity at a certain wavelength (R_λ) and specific detectivity (D^*) were used to evaluate the performance of the PD.[28] ($R_\lambda = \frac{I_l - I_d}{PA}$, where I_l is the light current, I_d is the dark current, P is the power density, and A is the effective light area) and ($D^* = \frac{R_\lambda}{(2eI_d/A)^{1/2}}$, e $=1.6\times10^{-19}$ C). R_λ denotes how efficiently a PD responds to optical signal, and D* means the ability to detect weak signals from a noisy environment. The PD1 exhibited broad-band self-powered photodetection performance from 300 to 530 nm with the highest R_λ (276 mAW^{-1}) and D^* (4.7×10^{11} Jones) attained at 530 nm, as shown in Figure 4e, which is superior than most of the reported PDs (Supplementary Table S1). In the meantime, the corresponding calculated values of external quantum efficiency (EQE) ($EQE\ (\%) = \frac{hcR_\lambda}{e\lambda}$) is as high as ~62 %. The PD1 demonstrated high stability with 96.8 % photocurrent retention even after a 200 cycles test (Figure 4f), laying the foundation for device applications. Furthermore, the PD demonstrated a fast response time with a rise time of 12 μs and decay time of 2.7 ms (Figure S7).

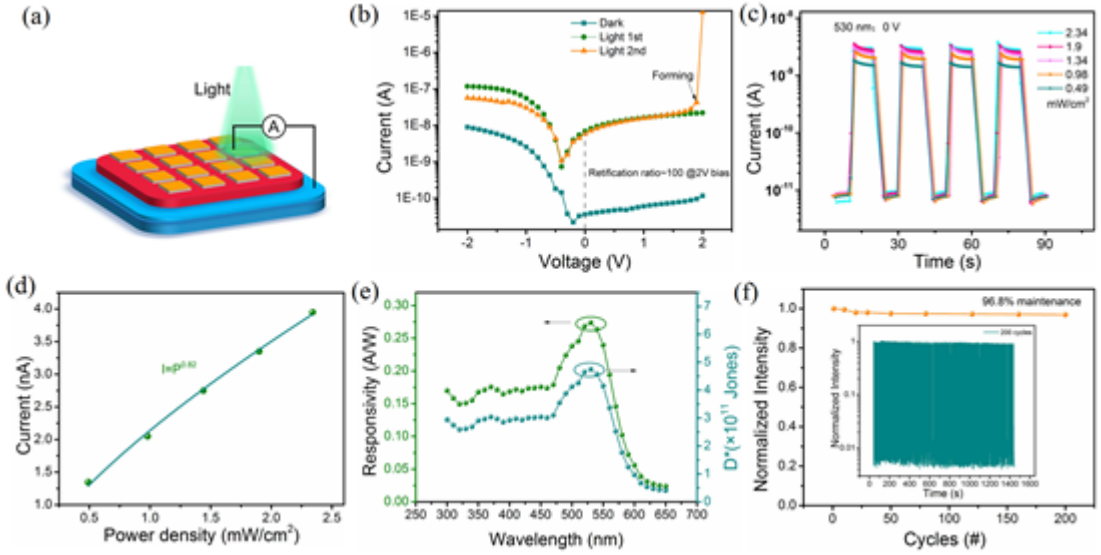

Figure 4 **a)** Schematic diagram of Au/Ag-$Cs_3Sb_2I_9$-ITO PD. And **b)** is the corresponding current voltage curves under dark and 530 nm light (2.34 $mWcm^{-2}$) and the electroforming of the memristor. **c)** Current time (I-T) curves of Au/Ag-$Cs_3Sb_2I_9$-ITO PD under different light intensities at 530 nm, and **d)** is the corresponding fitting curves. **e)** The responsivity and detectivity of the device. **f)** I-T curves with 200-cycle under 530 nm light.

To get a clear understanding of the I-V characteristics of the $Cs_3Sb_2I_9$-based RRAM device, a voltage sweeping cycle of 0 V → 0.5 V → 0 V → -0.5 V → 0 V was performed after the electroforming process (Figure 4b), as shown in Figure 5a. The ITO-$Cs_3Sb_2I_9$-Ag/Au ($Cs_3Sb_2I_9$ micro-plate thickness of ~2.4 μm) device displayed a bipolar resistive switching behaviors with a positive bias applied to the top electrode (Ag/Au) under a current compliance (Icc) of 10^{-5}A, where Au worked as an electrode protective layer over Ag.[29] During the switching process from 0 to 0.5 V, the device was initially in the high resistance state initially (HRS; 10^{-11} A), and underwent an abrupt switching to a low resistance state (LRS; 10^{-5} A) at a voltage of approximately + 0.15 V (V_{set}), while a negative voltage sweep (-0.5 to 0 V) reverted the LRS back to the initial HRS. It is such reversible feature that provides feasibility for the nonvolatile cyclic memristive operation. Furthermore, the thickness of the $Cs_3Sb_2I_9$ micro-plate had a significant influence on the operating voltage. As the thickness of the $Cs_3Sb_2I_9$ micro-plate decreases to 0.8 μm, the set voltage of $Cs_3Sb_2I_9$ RRAM device also decreases to 0.05 V (Figure S8). Figure S9 shows the statistical distribution of the set voltages for different thicknesses of $Cs_3Sb_2I_9$ micro-plate-based RRAM devices. The value of Vset increases with the

growing thickness of $Cs_3Sb_2I_9$ micro-plate, because the thicker $Cs_3Sb_2I_9$ micro-plate demands longer conductive filaments between pair electrodes, leading to harder resistive switching, as illustrated in Figure S10. Furthermore, because a thicker $Cs_3Sb_2I_9$ micro-plate has a higher resistance, it exhibits a higher on/off ratio than a thinner one under the same Icc. In the following investigation on endurance, the ITO-$Cs_3Sb_2I_9$-Ag/Au ($Cs_3Sb_2I_9$ micro-plate thickness of ~2.4 μm) device showed excellent consistency on I-V curves and had no attenuation after 60 successive cycle tests (Figure 5b). Data retention is a crucial parameter for evaluating RRAMs in practical applications. Here, the data retention characteristics, measured at V_{read} = 0.01 V for the ITO-$Cs_3Sb_2I_9$-Ag/Au ($Cs_3Sb_2I_9$ micro-plate thickness of ~2.4 μm) device, is shown in Figure 5c. For a sufficiently long period of > 7×10^3 s, the ITO-$Cs_3Sb_2I_9$-Ag/Au device retained its the HRS and LRS without degradation. Specifically, the HRS and LRS current were approximately 10^{-11}A and 10^{-6}A, respectively. The switching ratio of the device was concentrated at 10^5 within a retention time of > 7×10^3 s. Notably, the fabricated memristor demonstrated an outstanding SET power consumption as low as 3×10^{-11} W ($P_{set} = I_{set} \times V_{set}$). Compared with the on/off ratio and energy consumption of the state-of-the-art artificial neurons based on various materials, including two dimensional materials[30], $CsPbBr_3$ QDs[18] and other lead-free perovskites, the ITO-$Cs_3Sb_2I_9$-Ag/Au shows obvious competitiveness and advantages in terms of the on/off ratio and energy consumption (Figure 5e, Supplementary Table S2), exhibiting a high application potential in ultralow-power neuromorphic computing networks. Even after a long-term of memristor performance test, the device still maintained almost minimal attenuation of its light detection ability (Figure 5f), indicating that it has good repeatability and reusability.

The I-V characteristics were plotted on a double logarithmic scale (Figure 5d) to clarify the conducive principles of the HRS and LRS. The LRS fits linearly for log (I) versus log (V) with a slope of 1.02 during the positive sweep (+ 0.5 to 0 V; Figure S11), showing that the LRS state follows Ohmic conduction behavior. This is ascribed to the formation of the conducting filaments between the Ag/Au and ITO electrodes through the $Cs_3Sb_2I_9$ micro-plate, resulting a highly conducive LRS. Moreover, the conduction in the HRS can be divided into two segments (Figure S12 and S13): Ohmic contact ($I \propto V$) and Schottky contact ($Log(I) \propto V^{1/2}$)[30-33]. Initially, the migration of diffused cations (mainly Ag^+) from the Au/Ag is governed by the conduction mechanism of thermionic Schottky emission: $LnI \propto \sqrt{\frac{q^3}{4\varepsilon\pi d}}kT \times \sqrt{V}$ (I is the current, ε is the dielectric constant, q is the electrical charge, d is the thickness of $Cs_3Sb_2I_9$ micro-plate and V is the applied voltage). The observed

transition from the Schottky behavior to Ohmic behavior indicates that the unfilled trap centers are gradually seized by the charged carriers; therefore, the Schottky barrier is overcomed by ion migration and arrangement, leading to a larger current increment with the increased voltage. The resistive switching (RS) mechanism is summarized schematically in Figures 5g–j. From the vertical structure demonstrated in Figure 5g, with the increase of the bias voltage, Ag is easily oxidized into Ag ions ($Ag \rightarrow Ag^+ + e^-$), which gradually move from the Ag/Au to the ITO. After reaching the ITO, Ag^+ is reduced to Ag atoms, which accumulate and grow toward Ag/Au. Simultaneously, negatively charged I ions (I^-) in the micro-plate migrate to Ag/Au, leaving numerous I vacancies (V_I) to form local filaments (Figure 5h), corresponding to the electroforming process. After electroforming, the device was switched from the HRS to the LRS, and Ag and V_I were both components that formed a conductive filament (Figure 5i). When a negative voltage sweep (-0.5 to 0 V) is applied, oxidized Ag^+ ions migrate back towards the Ag/Au electrode and I^- moving in the opposite direction to the ITO electrode under the reverse electric field, leading to the rupture of the as-formed conductive filament (Figure 5j)[34,35]. The performance of the device as a memristor remained unchanged, and the photocurrent remained 57.3 % of its original level, even after 50 days in air condition (Figure S14). In addition, the Au/Ag/$Cs_3Bi_2I_9$/ITO device demonstrated a dual-functional ability, showing the universality of our method (Figure S15).

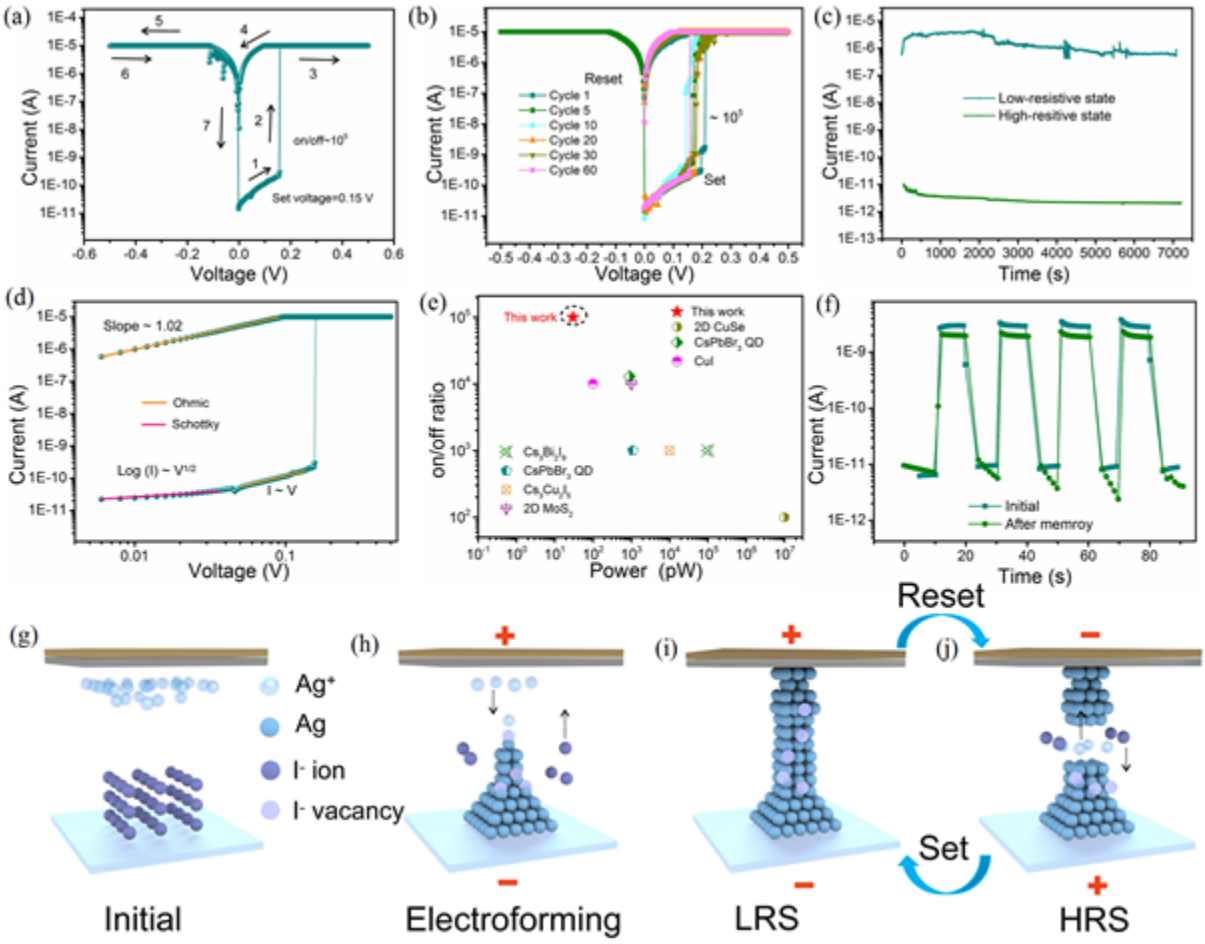

Figure 5 **a)** Typical cuttent voltage (I-V) curves of the memristor after the electroforming process. **b)** Resistive switching performing of the Au/Ag-$Cs_3Sb_2I_9$-ITO device of the 60-cycle sweeps. **c)** Retention test performance. **d)** Log (I) vs. log (V) plot of the I-V characteristics of Au/Ag-$Cs_3Sb_2I_9$-ITO device. **e)** Comparation of the main parameters (on/off ratio and power consumption) of our device and others in the literature. **f)** current time curves of Au/Ag-$Cs_3Sb_2I_9$-ITO devices before and after memory. **g, h)** The schematic of the resistive switching physical mechanism. **g)** Initial state, **h)** electroforming process, **i)** Low resistance states after SET process, and **j)** High resistance states after RESET process. (The thickness of the $Cs_3Sb_2I_9$ micro-plate is 2.4 μm)

3. Conclusion

We designed a dual-functional device with photoelectric detection and data storage capabilities that mimics the functions of the human visual memory. The PD based on lead-free $Cs_3Sb_2I_9$ micro-plates owns a high rectification ratio of ~100 (± 2V) and an ultra-high self-powered responsivity of 276 mAW^{-1} under 530 nm light. As a memristor, it demonstrated a forming step prior to repeating the switching, a low operating voltage (0.15 V), an ultra-high on/off ratio (~10^5), an ultra-low power consumption (3×10^{-11} W), and a long-term retention (> 7000 s) after 60 switching cycles. Light distribution with a patterned image can be detected and written in the visual memory arrays (4 × 4 pixels), mimicking the human visual memory to capture and store images. The stored information exhibited a long-term retention performance for over 60 minutes in the visual memory arrays owning to the nonvolatile characteristics of the resistance switching memristor. In addition, the visual memory arrays could be reprogrammed by a negative voltage reverse cycle, demonstrating their effective reusability. The design of a dual-functional device with photoelectric detection and data storage capabilities provides a novel approach for imitating the human visual memory, thereby creating new opportunities for visual memory devices to be utilized in future electronic eyes and other multifunctional applications.

4. Experimental Section

4.1 Fabrication of $Cs_3Sb_2I_9$ micro-plates on the substrates

1.5×1.5 cm ITO substrate was sequentially cleaned with water, ethanol in the ultrasonic bath, and dried with nitrogen. Before the growth process, 0.195 g CsI and 0.251 g SbI_3 were mixed and dissolved in 1 mL γ-butyrolactone (γ-GBL; 99.9 %) solvent, to prepare the solutions under 40 °C. The precipitations were removed by a 0.22 μm needle PTFE filter. 1 μl solution was transferred on the center of the glass, which was covered by the ITO substrate. The growth temperature was kept at 70 °C for 12 h. Adjusting the pressure between the glass and the ITO from 0 to 120 N with stationery folder (Figure S1).

4.2 Characterization of $Cs_3Sb_2I_9$ micro-plates

The crystal phase, size and morphology of $Cs_3Sb_2I_9$ micro-plates were determined by X-ray diffractometer (XRD, Cu-Kα radiation source, λ=0.15418 nm), optical microscopy (Olympus), field-

emission electron microscopy (FEI Nova NanoSEM 430), and transmission electron microscopy (TEM; JOEL JEM-2100F). AFM and KPFM images were obtained using Bruker Dimension Icon. The thickness of the $Cs_3Sb_2I_9$ micro-plates were conducted by Step Profiler. EDS mapping was used to collect the elemental information of the $Cs_3Sb_2I_9$ micro-plates. Focused-ion beam (FIB) measurement was conducted on FEI Strata 400S.

4.3 Fabrication and photoelectric measurements of photodetectors

Cu grids (300 meshes, with the square voids of 50 μm side size) were put on the top of $Cs_3Sb_2I_9$ micro-plates. Ag (~100 nm) and Au electrodes (~50 nm) were subsequently thermally evaporated on the sample. After removing the Cu grids, square-shaped electrodes with ~20 μm apart were successfully formed on the $Cs_3Sb_2I_9$ micro-plates. The photodetectors (PDs) with a thickness of 2.4 μm and 0.8 μm $Cs_3Sb_2I_9$ micro-plates are named as PD1 and PD2, respectively. The dual-functional device was performed by using a standard four-probe station with a Keithley 4200S semiconductor analyzer coupled with a 450 W Xe lamp equipped with a monochromator as the light source. And a 355 nm Q-switch Nd:YAG laser and the oscilloscope (Tektronix MSO/DPO5000) were used to record the transient photoresponse.

4.4 First principal calculation of the bandgap

Density functional theory (DFT) calculations were carried out for energy bandgap information. The exchange–correlation effects were handled using the generalized gradient approximation (GGA) of the Perdew-Burke-Ernzerhof (PBE). The interactions between core and valence electrons were described by the projector augmented wave (PAW) method. In addition, the Heyd–Scuseria–Ernzerhof (HSE06) method was used to correct the bandgap values, where a 25% of exact nonlocal Hartree-Fock exchange functional was added to the PBE functional. The structure relaxations were performed with a 520 eV plane-wave cutoff energy. The convergence criteria of supercell optimization for energy and force were set as 10^{-5} eV and 0.02 eV $Å^{-1}$, respectively.

Supporting Information

Supporting Information is available from the Wiley Online Library or from the author.

Acknowledgements

This work is supported by National Natural Science Foundation of China (No. 92263106, 12061131009 and 12211530438), the National Key R&D Program of China (No. 2018YFA0703700), the China Postdoctoral Science Foundation (2022M710710), Science and Technology Commission of Shanghai Municipality (No. 21520712600 and 19520744300).

Received: ((will be filled in by the editorial staff))

Revised: ((will be filled in by the editorial staff))

Published online: ((will be filled in by the editorial staff))

References

[1] S. Chen, Z. Lou, D. Chen, G. Shen, *Adv. Mater.* **2018**, 30, 1705400.

[2] Y. Liu, Z. Ji, G. Cen, H. Sun, H. Wang, C. Zhao, Z. L. Wang, W. Mai, *Light Sci. Appl.* **2023**, 12, 43.

[3] Z. Ji, Y. Liu, C. Zhao, Z. L. Wang, W. Mai, *Adv. Mater.* **2022**, 34, 2206957.

[4] J. Feng, C. Gong, H. Gao, W. Wen, Y. Gong, X. Jiang, B. Zhang, Y. Wu, Y. Wu, H. Fu, L. Jiang, X. Zhang, *Nat. Electron.* **2018**, 1, 404.

[5] a) F. Zeng, Y. Guo, W. Hu, Y. Tan, X. Zhang, J. Feng, X. Tang, *ACS Appl. Mater. Interfaces* **2020**, 12, 23094; b) G. S. Syed, Y. Zhou, J. Warner, H. Bhaskaran, *Nat. Nanotechnol.* **2023**. DOI: 10.1038/s41565-023-01391-6.

[6] Y. Zhong, J. Tang, X. Li, X. Liang, Z. Liu, Y. Li, Y. Xi, P. Yao, Z. Hao, B. Gao, H. Qian, H. Wu, *Nat. Electron.* **2022**, 5, 672.

[7] L. Yin, R. Cheng, Y. Wen, C. Liu, J. He, *Adv. Mater.* **2021**, 33, 2007081.

[8] a) X. Chen, W.-g. Lu, J. Tang, Y. Zhang, Y. Wang, G. D. Scholes, H. Zhong, *Nat. Photonics.* **2021**, 15, 813; b) F. Cao, T. T. Yan, Z. Q. Li, L. M. Wu, X. S. Fang, *Adv. Opt. Mater*. **2022**,10, 2200786.

[9] J. Wang, J. Li, S. Lan,C. Fang, H. Shen, Q. Xiong, D. Li, *ACS Nano* **2019**, 13, 5473.

[10] J. X. Chen, X. Y. Liu, Z. Q. Li, F. Cao, X. Lu, X. S. Fang, *Adv. Funct. Mater.* **2022**, 32, 2201066.

[11] a) P. Zhao, M. Cui, Y. Li, J. Lao, C. Jiang, C. Luo, B. Tian, H. Lin, H. Peng, C. Duan, *J. Mater. Chem. C* **2023**, 11, 6212. b) J. Lao, M. Yan, B. Tian, C. Jiang, C. Luo, Z. Xie, Q. Zhu, Z. Bao, N. Zhong, X. Tang, L. Sun, G. Wu, J. Wang, H. Peng, J. Chu, C. Duan, *Adv. Sci*. **2022**, 9, 2106092.

[12] a) H. Ye, Z. Liu, B. Sun, X. Zhang, T. Shi, G. Liao, *Adv. Electron. Mater*. **2022**, 9, 2200657. b) H. Kim, W. Kim, Y. Pak, T. J. Yoo, H. W. Lee, B. H. Lee, S. Kwon, G. Y. Jung, *Laser Photonics Rev.* **2020**, 14, 2000305.

[13] a) Y. Liu, Y. Zhang, X. Zhu, Z. Yang, W. Ke, J. Feng, X. Ren, K. Zhao, M. Liu, M. G. Kanatzidis, S. Liu, *Sci. Adv.* **2021**, 7, eabc8844. b) H. P. Wang, S. Y. Li, X. Y. Liu, Z. F. Shi, X. S. Fang, J. H. He, *Adv. Mater*. **2021**, 33, 2003309.

[14] W. Kim, H. Kim, T. J. Yoo, J. Y. Lee, J. Y. Jo, B. H. Lee, A. A. Sasikala, G. Y. Jung, Y. Pak, *Nat. Commun.* **2022**, 13, 720.

[15] a) S.-X. Li, Y.-S. Xu, C.-L. Li, Q. Guo, G. Wang, H. Xia, H.-H. Fang, L. Shen, H.-B. Sun, *Adv. Mater.* **2020**, 32, 2001998; b) F. Cao, Z. Li, X. Liu, Z. Shi, X. S. Fang, *Adv. Funct. Mater*. **2022**, 32, 2206151.

[16] R. S. Kei Hirose, J. Hernlund, *Science* **2017**, 358, 734.

[17] H. Sun, W. Tian, X. Wang, K. Deng, J. Xiong, L. Li, *Adv. Mater.* **2020**, 32, 1908108.

[18] M. C. Yen, C. J. Lee, K. H. Liu, Y. Peng, J. Leng, T. H. Chang, C. C. Chang, K. Tamada, Y. J. Lee, *Nat. Commun.* **2021**, 12, 4460.

[19] Z. Xiong, W. Hu, Y. She, Q. Lin, L. Hu, X. Tang, K. Sun, *ACS Appl. Mater. Interfaces* **2019**, 11, 30037.

[20] a) S. K. Shil, F. Wang, Z. Lai, Y. Meng, Y. Wang, D. Zhao, M. K. Hossain, K. O. Egbo, Y. Wang, K. M. Yu, J. C. Ho, *Nano Res.* **2021**, 14, 4116. b) F. Cao, X. Deng, X. Liu, L. Su, E. Hong, L. Wu, X. S. Fang, *ACS Appl. Mater. Interfaces* **2023**, 15, 28158.

[21] S. K. Shil, F. Wang, K. O. Egbo, Z. Lai, Y. Wang, Y. Wang, D. Zhao, S. W. Tsang, J. C. Ho, K. M. Yu, *ACS Appl. Mater. Interfaces* **2021**, 13, 35930.

[22] Z. Li, X. Liu, C. Zuo, W. Yang, X. S. Fang, *Adv. Mater*. **2021**, 33, 2103010.

[23] C. Yang, B. Sun, G. Zhou, T. Guo, C. Ke, Y. Chen, J. Shao, Y. Zhao, H. Wang, *ACS Mater. Lett.* **2023**, 5, 504.

[24] B. Saparov, F. Hong, J.-P. Sun, H.-S. Duan, W. Meng, S. Cameron, I. G. Hill, Y. Yan, D. B. Mitzi, *Chem. Mater.* **2015**, 27, 5622.

[25] T. Geng, Z. Ma, Y. Chen, Y. Cao, P. Lv, N. Li, G. Xiao, *Nanoscale* **2020**, 12, 1425.

[26] F. Cao, T.Wang, and X. Ji, *Appl. Surf. Sci.* **2019**, 471, 417.

[27] W. D. Song, J. Chen, Z. Li, X. S. Fang, *Adv. Mater.* **2021**, 33, 2101059.

[28] F. Cao, L. Jin, Y. Wu, X. Ji, *J. Alloy. Compd.* **2021**, 859, 158383.

[29] L. Li, Y. Chen, C. Cai, P. Ma, H. Ji, G. Zou, *Small* **2022**, 18, 2103881.

[30] P. Lei, H. Duan, L. Qin, X. Wei, R. Tao, Z. Wang, F. Guo, M. Song, W. Jie, J. Hao, *Adv. Funct. Mater*. **2022**, 32, 2201276.

[31] X. Liu, S. Ren, Z. Li, J. Guo, S. Yi, Z. Yang, W. Hao, R. Li, J. Zhao, *Adv. Funct. Mater*. **2022**, 32, 2202951.

[32] T. Wang, J. Meng, X. Zhou, Y. Liu, Z. He, Q. Han, Q. Li, J. Yu, Z. Li, Y. Liu, H. Zhu, Q. Sun, D. W. Zhang, P. Chen, H. Peng, L. Chen, *Nat. Commun.* **2022**, 13, 7432.

[33] D. Mishra, K. Mokurala, A. Kumar, S. G. Seo, H. B. Jo, S. H. Jin, *Adv. Funct. Mater*. **2022**, 33, 2211022.

[34] F. Xue, C. Zhang, Y. Ma, Y. Wen, X. He, B. Yu, X. Zhang, *Adv. Mater.* **2022**, 34, 2201880.

[35] a) J. Ma, H. Liu, N. Yang, J. Zou, S. Lin, Y. Zhang, X. Zhang, J. Guo, H. Wang, *Adv. Mater.* **2022**, 34, 2202371; b) J. Park, D. Seong, Y. J. Park, S. H. Park, H. Jung, Y. Kim, H. W. Baac, M. Shin, S. Lee, M. Lee, D. Son, *Nat. Commun.* **2022**, 13, 5233.

In this work, inspired by the function of human visual memory, we designed a dual-functional perovskite-based photodetector (PD) and memristor, realizing visual perception and memory capacities. An ultra-high self-powered responsivity of 276 mAW^{-1}, and a high detectivity of 4.7×10^{11} Jones for a PD and an ultra-high on/off ratio (~10^5), an ultra-low power consumption of 3×10^{-11} W, a low setting voltage (0.15 V) and long retention time (>7000 s) for a memristor are realized by the dual-functional device. Such device provides new opportunities for the mimicry of human visual memory in future multifunctional application.

Keywords: Dual-functional; perovskite; photodetector; memristor; visual memory.

Fa Cao, Zijun Hu, Tingting Yan, Enliu Hong, Xiaolei Deng, Limin Wu* and Xiaosheng Fang*

Dual-functional Perovskite-based Photodetector and Memristor for Visual Memory